EXPLOSIVE EVENTS IN THE SOLAR TRANSITION ZONE

K. P. DERE, J.-D. F. BARTOE, and G. E. BRUECKNER

E.O. Hulburt Center for Space Research, Naval Research Laboratory, Washington, D.C. 20375, U.S.A.

Abstract. The properties of explosive events in the solar transition zone are presented by means of detailed examples and statistical analyses. These events are observed as regions of exceptionally high velocity (~ 100 km s^{-1}) in profiles of CIV, formed at 10^5 K, observed with the High Resolution Telescope and Spectrograph (HRTS). The following average properties have been determined from observations obtained during the third rocket flight of the HRTS: full width at half maximum extent along the slit – 1.6×10^3 km; maximum velocity – 110 km s^{-1}; peak emission measure – 4×10^{41} cm^{-3}; lifetime – 60 s; birthrate – 4×10^{-21} cm^{-2} s^{-1} in a coronal hole and 1×10^{-20} cm^{-2} s^{-1} in the quiet Sun; mass – 6×10^8 g; and, kinetic energy – 6×10^{22} erg. The 6 examples show that there are considerable variations from these average parameters in individual events. Although small, the events show considerable spatial structure and are not point-like objects. A spatial separation is often detected between the positions of the red and blue shifted components and consequently the profile cannot be explained by turbulence alone. Mass motions in the events appear to be isotropic because the maximum observed velocity does not show any correlation with heliographic latitude. Apparent motions of the 100 km s^{-1} plasmas during their 60 s lifetime should be detected but none are seen. The spatial frequency of occurrence shows a maximum near latitudes of $40-50°$, but otherwise their sites seem to be randomly distributed. There is enough mass in the explosive events that they could make a substantial contribution to the solar wind. It is hard to explain the heating of typical quiet structures by the release of energy in explosive events.

1. Introduction

One of the major discoveries made with the NRL High Resolution Telescope and Spectrograph (HRTS) during its first rocket flight in 1975 was the occurrence of high-velocity (100–400 km s^{-1}) events seen in transition zone lines. After the first two rocket flights, it became clear that these events were quite common. The first analysis of the high velocity events (Brueckner and Bartoe, 1983) classified these events into two categories, turbulent events and jets and concentrated on their overall role in the source and energetics of the outer solar atmosphere. The results of the first two rocket flights indicated that it was important to have data covering an extended area of the solar surface in order to understand their role in the transport of mass, momentum, and energy in the outer solar atmosphere. To accomplish this, the observing program for the third rocket flight (HRTS-3) performed repeated rasters of a $10'' \times 800''$ region of the Sun. In this paper, a detailed analysis of several events and a statistical analysis of 82 events observed during this rocket flight are presented. One purpose of presenting the complete spectra of selected events is to demonstrate the range of variation of the phenomena. The HRTS-3 data set contains no examples of the 400 km s^{-1} jets reported by Brueckner and Bartoe (1983) but only examples of what they termed 'turbulent' events. The analysis to be presented will also show that the properties implied by the term 'turbulent' do not describe these wide profile events perhaps as well as the term 'explosive' which we have used in the past (Dere, Bartoe, and Brueckner, 1984).

Recently, Cook *et al.* (1988) have presented a statistical analysis of the explosive events observed during the Spacelab 2 mission in 1985.

2. The Data

The data used in this analysis was obtained during the third rocket flight of the HRTS instrument on 1979 March 1 at 16:46 UT. Considerable effort has gone into reducing and analyzing this data set so that it is now well understood. A series of papers (Dere, Bartoe, and Brueckner, 1984, 1986a, b) describe in detail the reduction techniques applied to the data and provide a useful background on the ultraviolet structure of the solar features observed.

Briefly, the HRTS-3 instrument consists of a Cassegrain telescope which focuses an image of the Sun onto the slit jaws of a tandem-Wadsworth spectrograph which records the stigmatic spectrum between 1500 and 1600 Å on photographic film. The slit is roughly 1 solar radius long and a spatial resolution of 1″ along the slit is obtained. The slit has an equivalent width of 1″ which produces a corresponding spectral resolution of 0.1 Å. During the third rocket flight, the slit was pointed along a solar radius, with one end intersecting the limb at the south solar pole and the other end about 800″ inside the limb. Consecutive 3 s exposures were made at 6 raster positions separated by 2″ to cover a solar area 10″ × 800″. This sequence was repeated every 20 s until the end of the rocket flight and resulted in 10 complete and 1 partial raster of the solar area over a period of about 200 s. The flight took place near sunspot maximum. The polar coronal hole showed an extension down to a solar latitude of about 55° at the position of the slit. The other end of the slit subtended a decaying active region and a filament but most of the area covered showed features typical of the quiet Sun. The Kitt Peak magnetogram is not available for the day of the flight.

3. Examples of Explosive Events

While all explosive events are characterized by small sizes and high velocities, they often exhibit considerable variation in their spectral signature and its evolution from event to event. An appreciation of their range of variation is helpful before attempting to arrive at a coherent understanding of their physical nature. To this end, we present the spectra of 6 explosive events in detail before considering the properties of explosive events on a statistical basis.

3.1. EXAMPLE 1 (680)

In Figure 1, the complete sequence of profiles, obtained in the region containing the most dramatic explosive event in the data set, are shown. Each unit of this figure is a section of a stigmatic HRTS spectrum of summed C IV λ1548 and λ1550 profiles. Each displays spectra along a 16″ section of the slit and Doppler velocities from 155 km s^{-1} (blue) to 155 km s^{-1} (red). Blue shifts are to the left and red shifts to the right. Above and below each spectrum are tic marks indicating the position of zero velocity derived from
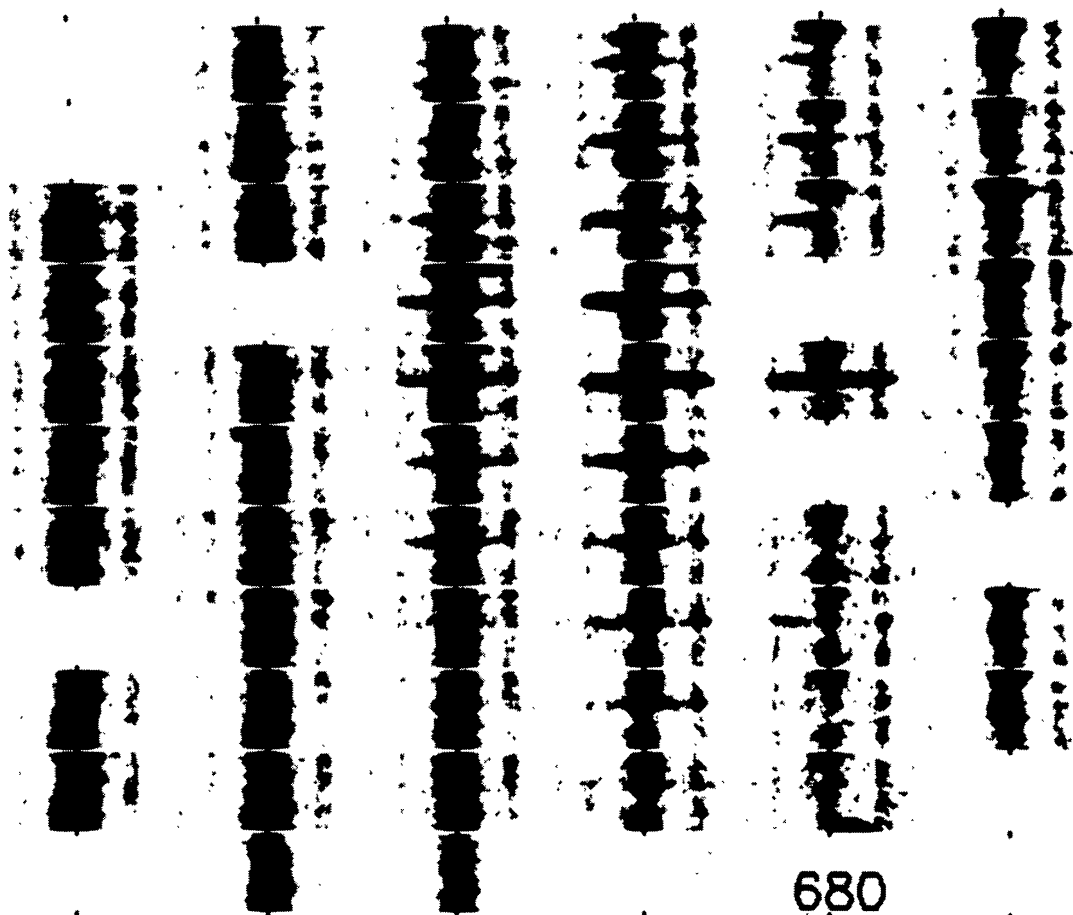
Fig. 1. The complete set of stigmatic C IV spectra for explosive event No. 1 (680). Each image is a 16″ portion of a stigmatic spectrum along the slit of summed C IV 1548 Å and 1550 Å profiles for velocities up to 150 km s^{-1}. These were obtained by stepping the slit in 2″ increments to make 6 exposures in each raster sequence which was repeated every 20 s. Displacements from left to right in the figure correspond to 2″ spatial steps and displacements from top to bottom in the figure correspond to 20 s in elapsed time.

the position of chromospheric Si I lines. From top to bottom there are 11 complete or partial raster sequences with time increasing from top to bottom. From left to right are 6 raster positions corresponding to displacements of the slit in 2″ increments. Each exposure lasted 3 s and it took 20 s to complete a spatial raster sequence. Consequently there is a 20 s interval between two sequential exposures at the same spatial position.

This example shows the presence of both strong blueshifted and redshifted material at the same location with velocities in both wings up to about 100 km s^{-1}. As in most explosive events, the profile is dominated by the intense, slowly evolving component at low velocities. There are two sequential brightenings of this event, the second being the weaker of the two. Profiles in the rise phase of the first brightening are shown in Figure 2 and profiles in the decay phase are shown in Figure 3. All of these profiles are from the fourth raster sequence from the left as seen in Figure 1. The profiles are labelled according to the raster sequence from which the data were taken. Raster sequence 6 was
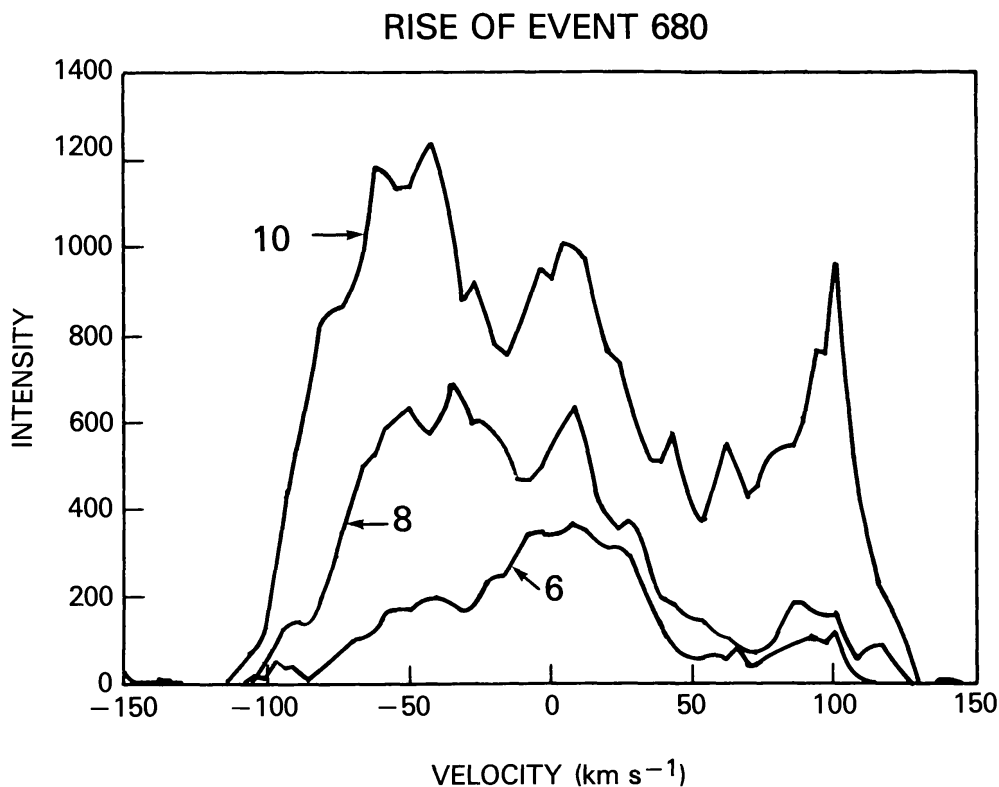
RISE OF EVENT 680

Fig. 2. C IV profiles during the rise phase of explosive event No. 1.
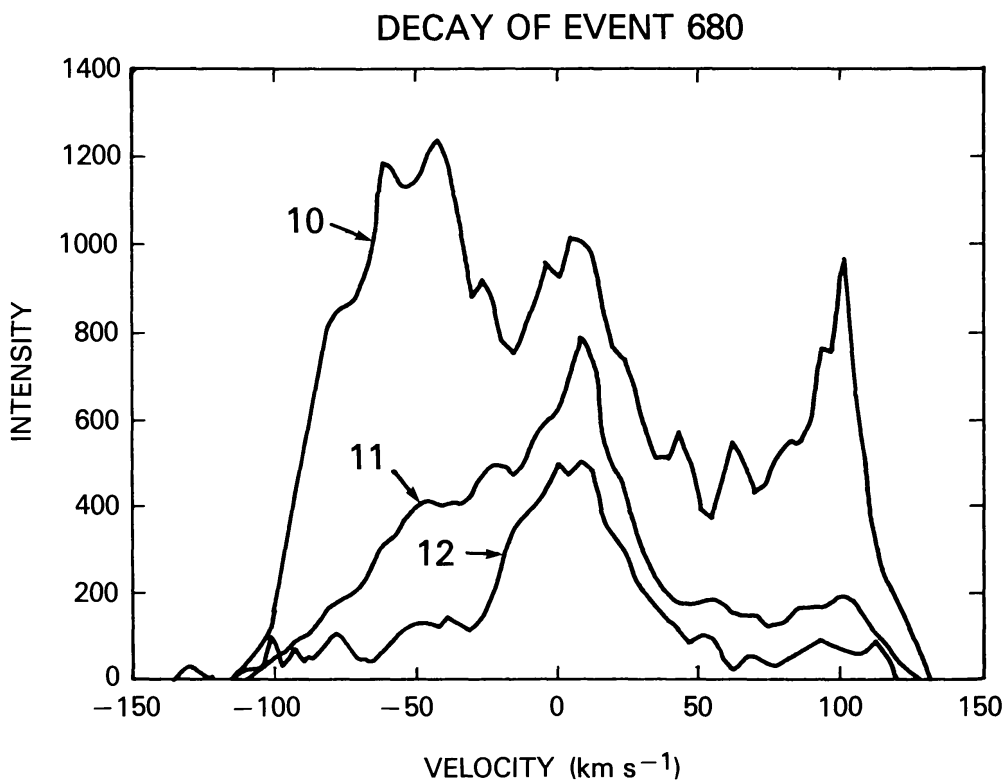
DECAY OF EVENT 680

Fig. 3. C IV profiles during the decay phase of explosive event No. 1.

the first obtained during the period of stable pointing and is the first seen at the top in Figure 1. The time difference between raster 6 and raster 8 is 40 s and between raster 8 and 10 is also 40 s. The elapsed time between profiles displayed in the decay phase is 20 s. At maximum phase, raster 9, the blue wing profile shows a peak in intensity at 50 km s^{-1}, with a rapid fall off at velocities above 90 km s^{-1} and below 40 km s^{-1}. At earlier and later times, the shape of the blue wing shows a flatter distribution of intensity with velocity. The profile of the red wing at maximum reveals a distinct spike at a velocity of 100 km s^{-1}. Although there are Si I lines at these equivalent Doppler shifts, they do not contribute enough intensity to be the dominant source of emission in the red wing. The profiles (Figures 2 and 3) indicate that the peak observed velocities are nearly constant throughout the event and the emission at lower velocities shows the greatest variation. The development of the profile cannot be interpreted as a simple acceleration and deceleration of plasmas. A time history of the integrated intensities in the red and blue wings is shown in Figure 4. The decay of both wings occurs more rapidly than their rise and both wings show a similar evolution in intensity.
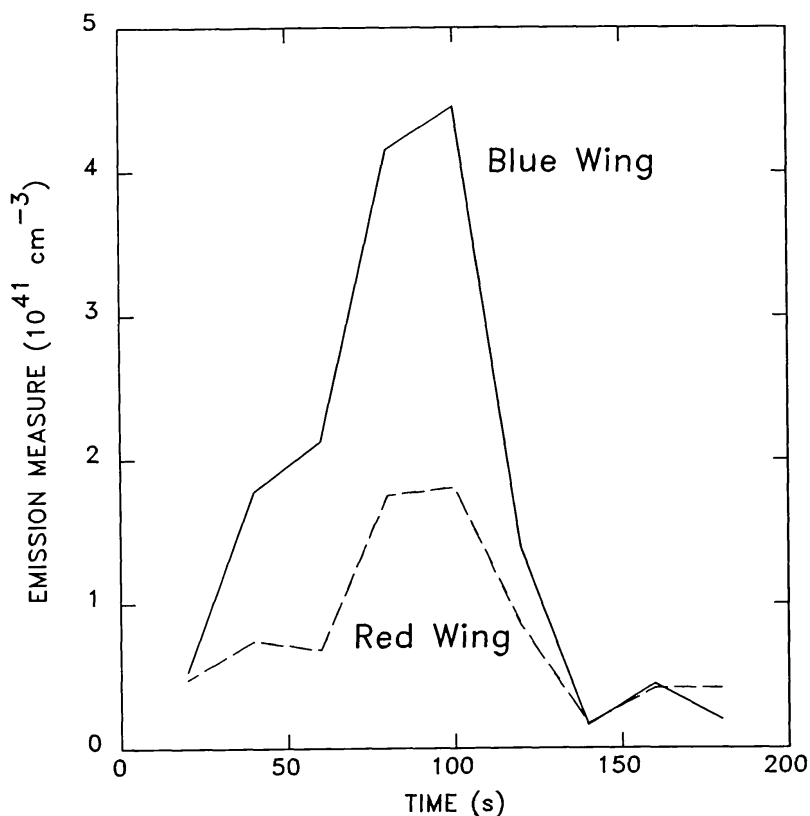

Fig. 4. Time histories of integrated intensities in the red and blue wing of C IV for explosive event No. 1.

3.2. EXAMPLE 2 (357)

The stigmatic C IV profiles obtained in the vicinity of explosive event example 2 are shown in Figure 5. This example consists of multiple events, with the first occurring early in the observing period, in the second and third raster position from the left, and the

Fig. 5. Stigmatic C IV spectra for explosive event No. 2 (357). See caption to Figure 1.

second occurring roughly 160 s later near the end of our observing period. In the intervening period, there is evidence of slightly enhanced line width at the same position. In Figure 6, the profile in the second raster position from the left in the second raster sequence is plotted. The emission in the high-velocity wings is approximately flat between the maximum velocities of 100 km s^{-1}.

3.3. EXAMPLES 3a AND 3b (461)

Two examples of explosive events occur in the same area and their stigmatic profiles are shown in Figure 7. Example 3a is prominent early in the observing period at raster positions 2 and 3 from the left. Its profile in the second raster sequence, third raster position, is shown in Figure 8. Near line center, both the C IV λ1548 and λ1550 profiles are over-exposed and are not displayed. This same condition can be seen in Figure 7 and others of the same format as scattered bright specks near line center in regions of exceptionally high intensity. The blue wing is clearly much brighter than the red and is characterized by a decreasing intensity with increasing blue shift up to a maximum velocity of 135 km s^{-1}. Although the highest velocities are found early in our observations, the event endures throughout our observing period at reduced strength.
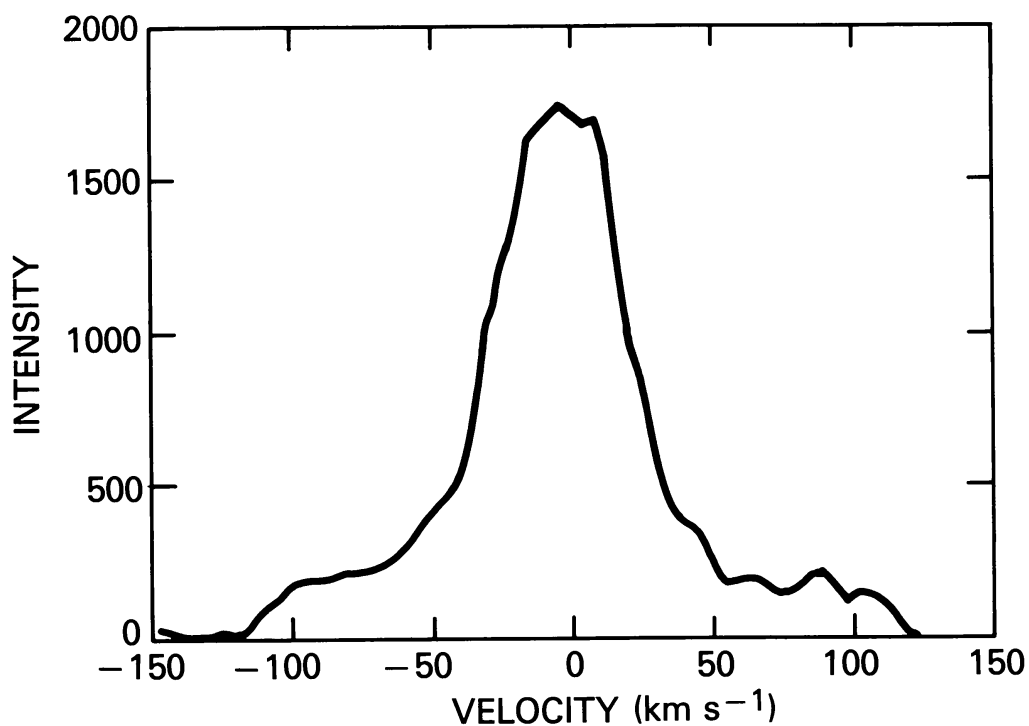
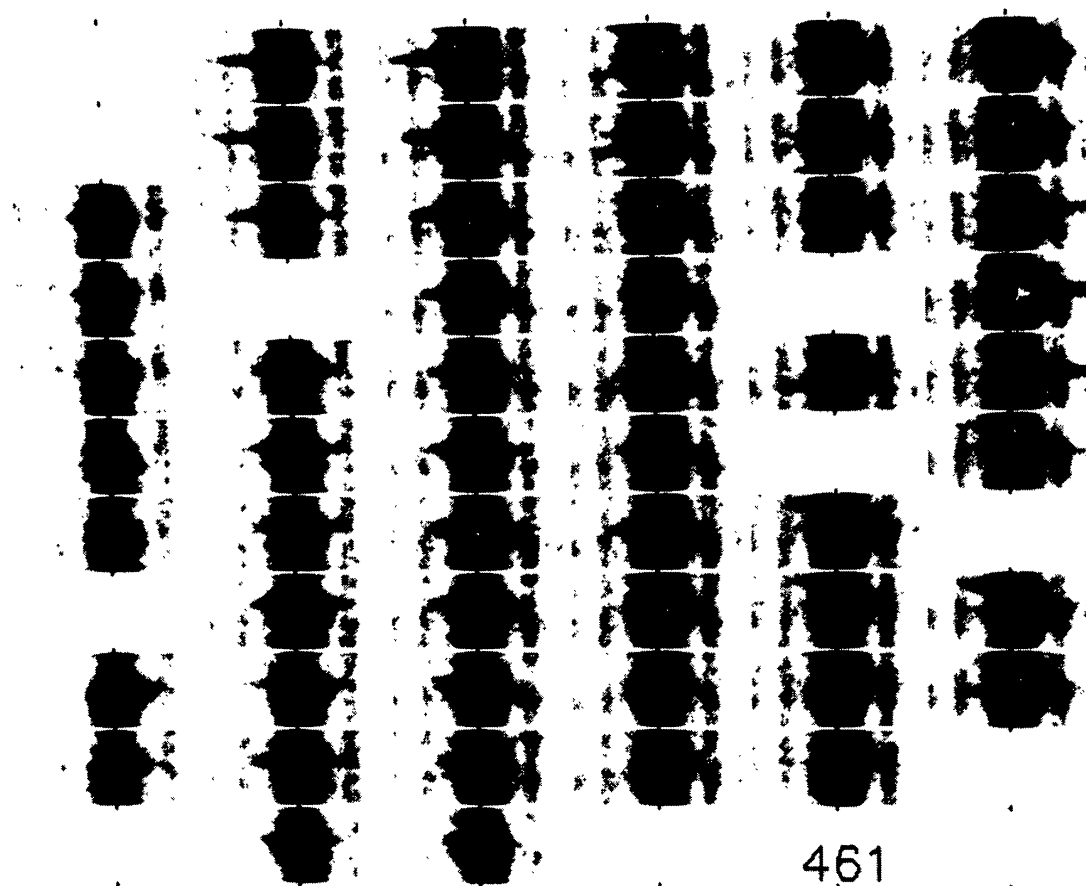Fig. 6. The profile of C IV during the maximum phase of event No. 2 (357).

Fig. 7. Stigmatic C IV spectra for explosive events Nos. 3a and 3b (461). See caption to Figure 1.
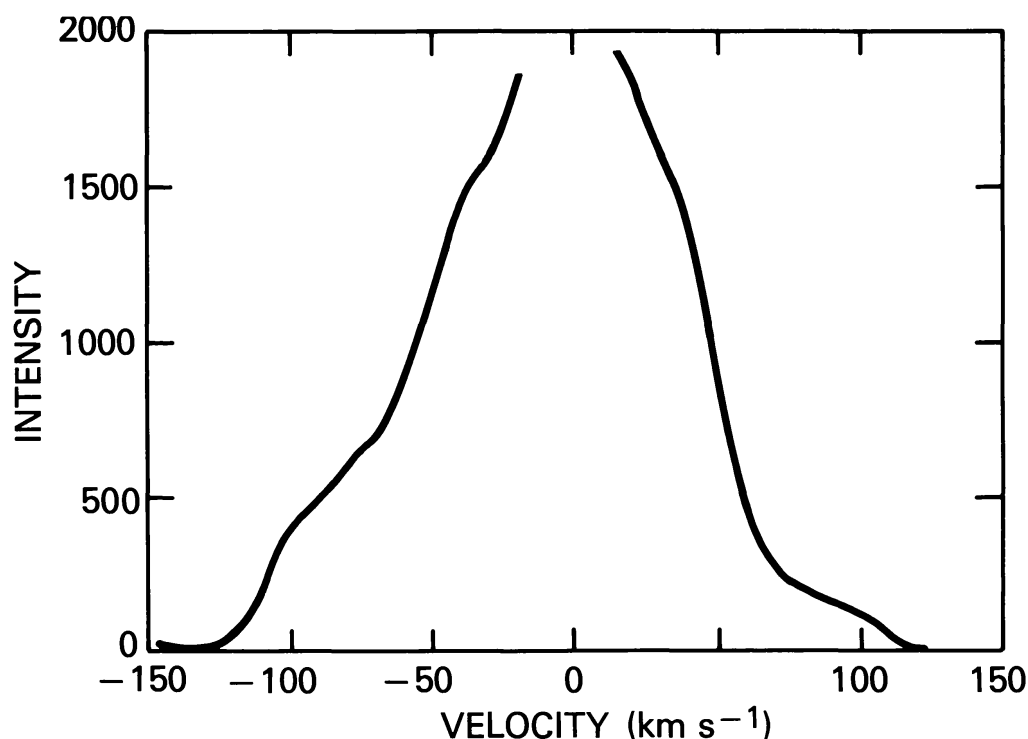
Fig. 8.   The profile of C IV during the maximum phase of event No. 3a (461).

Example 3b is seen in the sixth raster position, on the far right in Figure 7. The velocities at maximum phase are somewhat higher than can be displayed in the format used for these figures. The profile of this event in the second raster sequence is shown in Figure 9 where velocities up to about 225 km s^{-1} are evident in the red wing. The blue component is quite weak. This example develops quite rapidly and is also evident at low intensity throughout the observing period.

3.4. EXAMPLE 4 (869)

An example of an intense but short-lived event is shown at raster position 6 in Figure 10. The blue wing is fairly weak, especially compared with the very bright red wing. The event occurs in a small region that exhibits relatively enhanced brightness throughout the observing period and enhanced line width throughout a substantial part of this period. The profile at maximum phase is shown in Figure 11 where velocities up to 160 km s^{-1} are evident. During the 20 s between raster sequences 3 and 4, the maximum velocity increases from roughly 80 km s^{-1} to 160 km s^{-1}. This corresponds to an acceleration of 4 km s^{-2} which is near the value of 5 km s^{-2} found by Brueckner and Bartoe (1983) for the much faster coronal jets.

3.5. EXAMPLE 5 (976)

Figure 12 displays a long-lived mainly blue shifted event in raster positions 5 and 6. Significant spatial variation in the profile are evident. In the fifth raster position from the left in the early rasters, there is a velocity gradient along the slit with the greatest
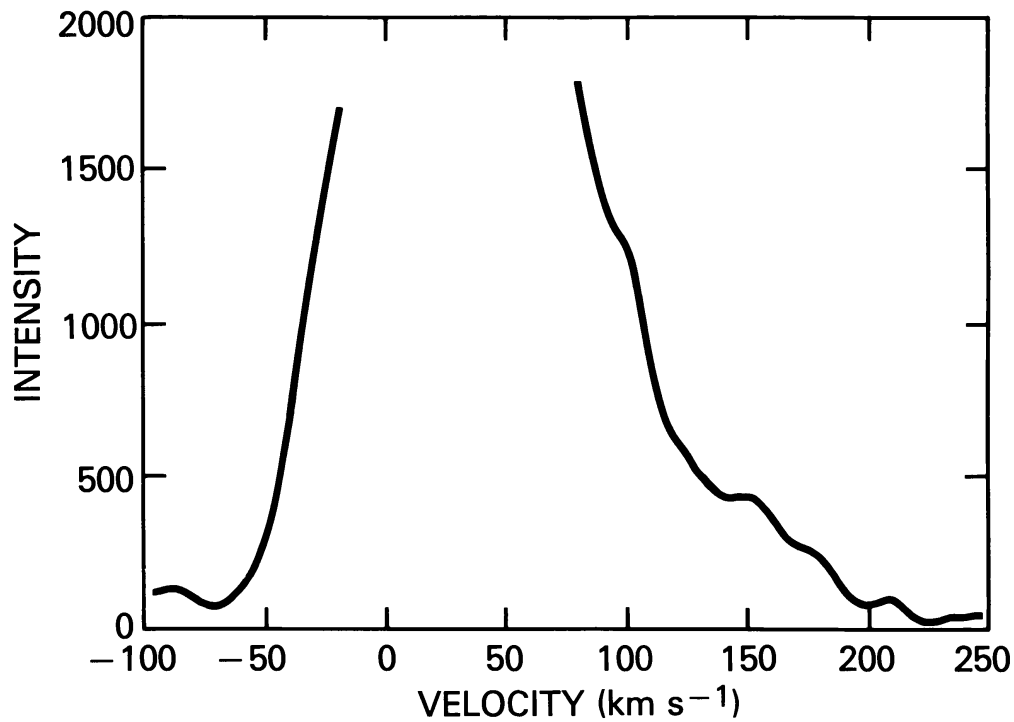
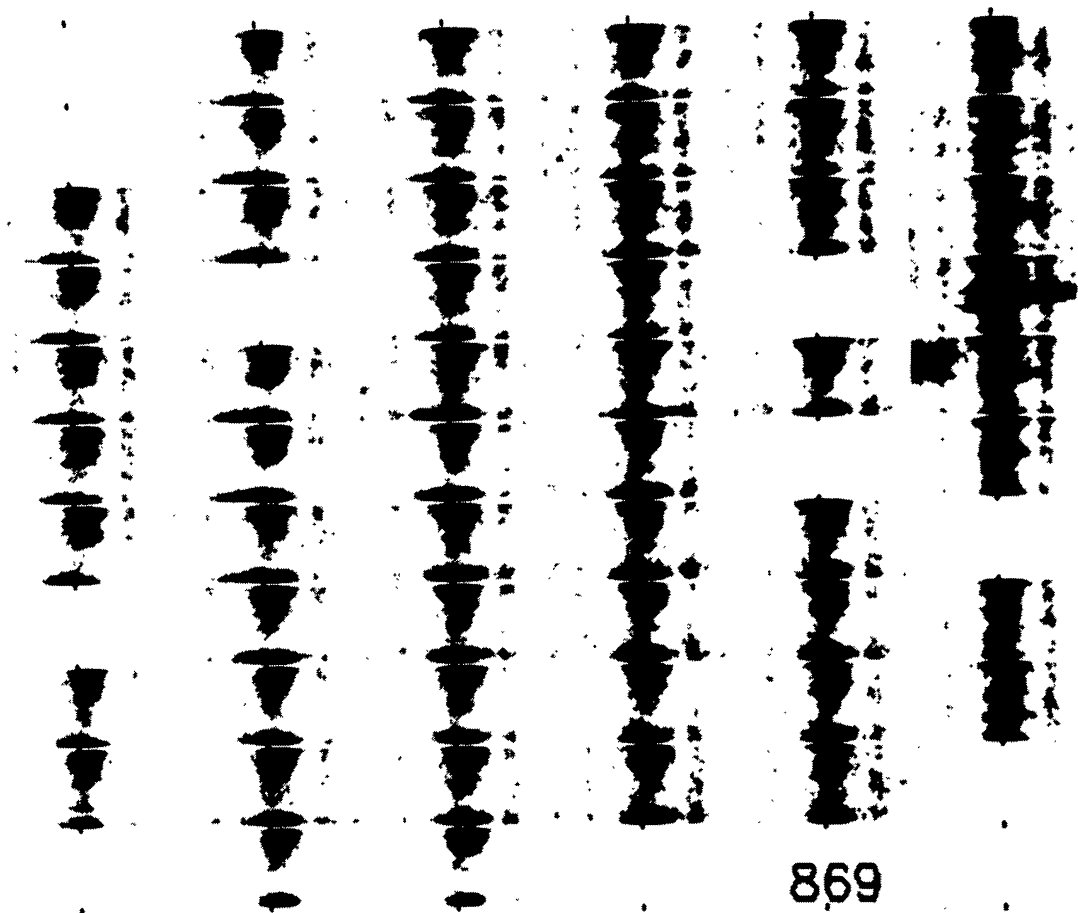Fig. 9. The profile of C IV during the maximum phase of event No. 3b (461).

Fig. 10. Stigmatic C IV spectra for explosive event No. 4 (869). See caption to Figure 1.
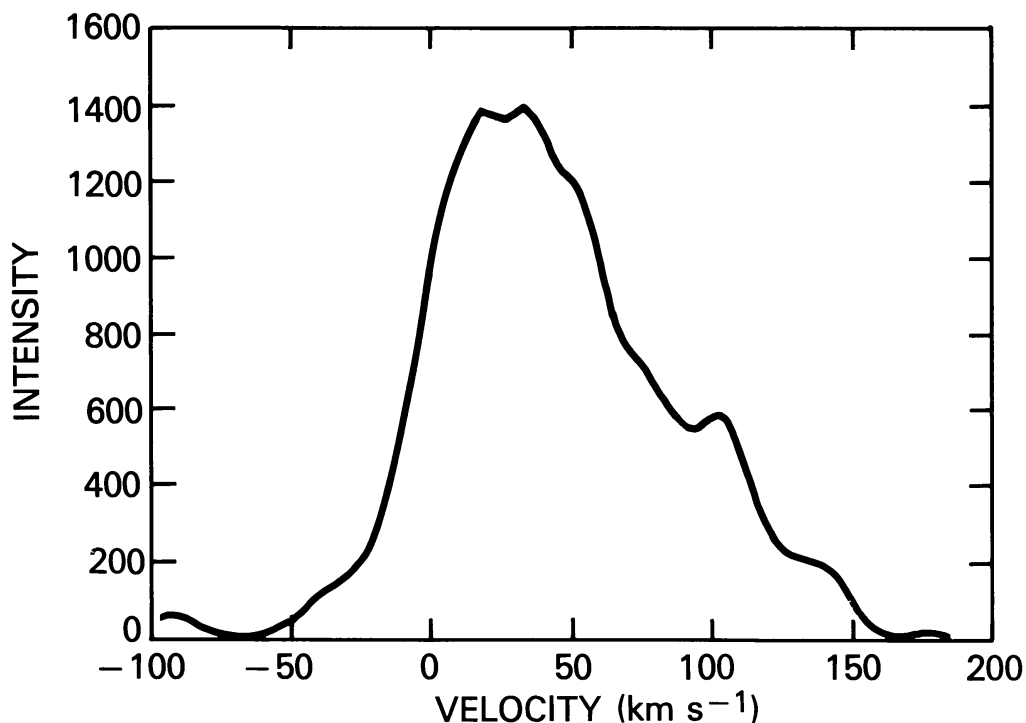
Fig. 11.   The profile of C IV during the maximum phase of event No. 4 (869).
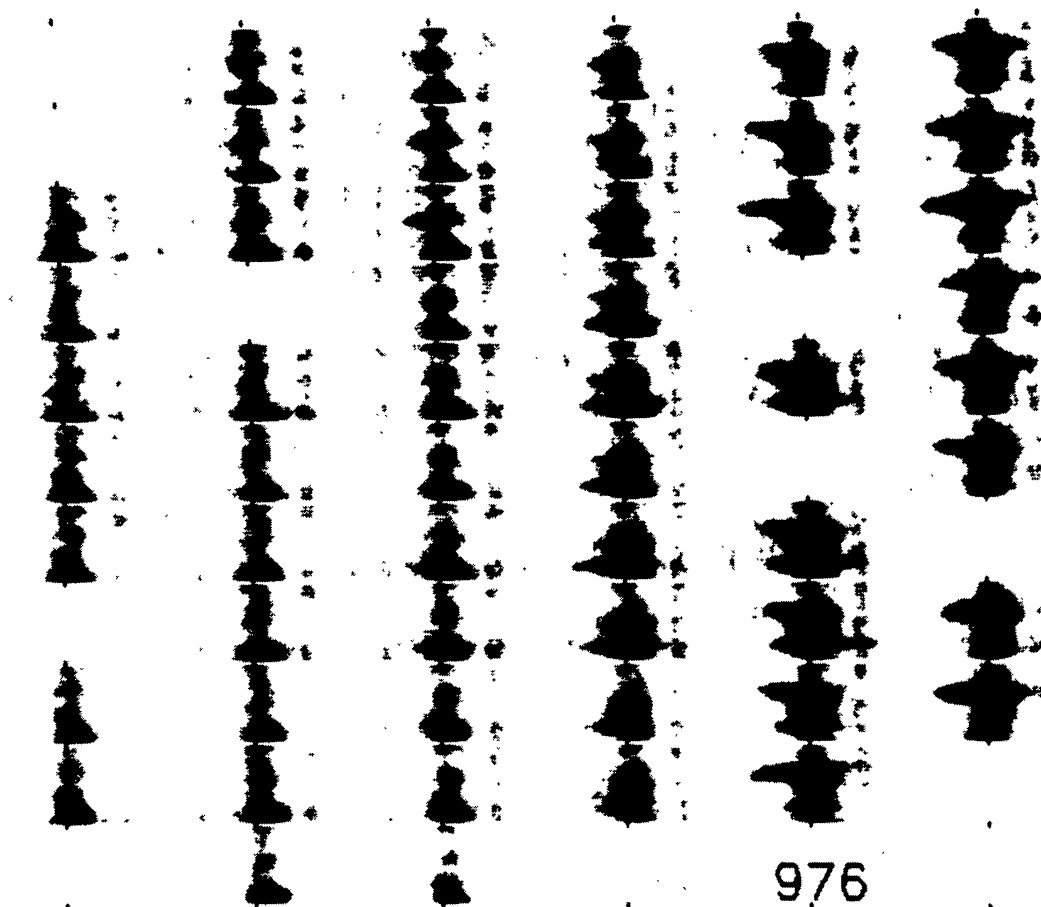
Fig. 12.   Stigmatic C IV spectra for explosive event No. 5 (976). See caption to Figure 1.

velocities attained toward the top of the figure. There are also strong changes in the red wing in the 2″ between raster positions 5 and 6. The profile of this event at raster position 6 in the third raster sequence is shown in Figure 13 where blueward velocities up to 125 km s^{-1} are found. Sequential intensity and velocity images of this event have been examined before by Dere, Bartoe, and Brueckner (1986b) where it was referred to as example 9a.
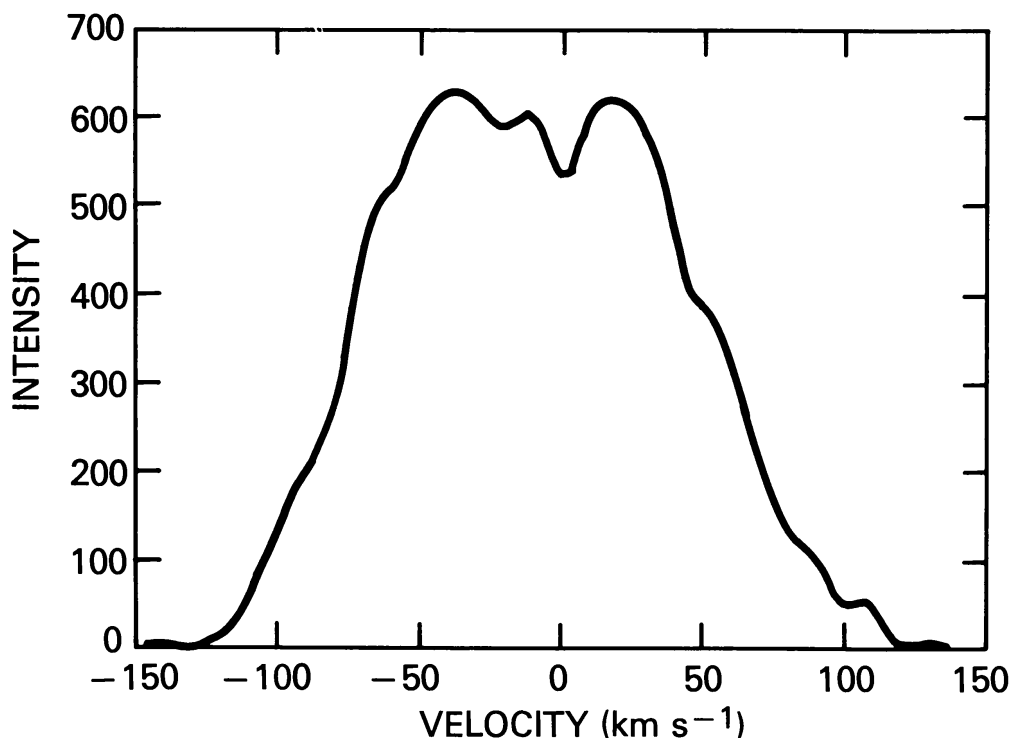
Fig. 13. The profile of C IV during the maximum phase of event No. 5 (976).

3.6. EXAMPLE 6 (1660)

Stigmatic profiles of example 8 are shown in Figure 14. This is the only explosive event which occurred in an old active region near Sun center. The event occurred at raster position 6 which is the only one displayed in Figure 14 in order to completely show the exceptionally wide profiles. The profiles shown changes in each consecutive exposure and the maximum phase is very short. The profile at maximum is shown in Figure 15. If the effects of blends and of the normal background C IV component are disregarded, the profile is nearly symmetric and one of the few profiles of an explosive event which could be attributed to isotropic turbulence, although earlier profiles in this event are not symmetric.

3.7. SUMMARY

The 6 examples have been chosen from 82 observed explosive events to illustrate the common characteristics of the phenomena as well as the wide range of variation found from event to event. The explosive events are small with sizes near 2″ but often show
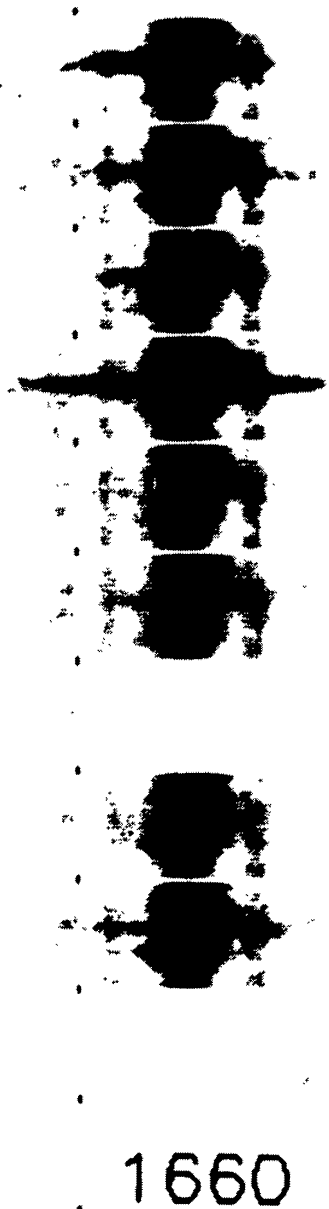
Fig. 14.   Stigmatic C IV spectra for explosive event No. 6 (1660). See caption to Figure 1.

considerable structural variation on these scales. The profiles typically reveal velocities up to about 100 km s^{-1} and sometimes greater than 200 km s^{-1}. Both red and blue shifted components are seen but one wing is often clearly dominant and sometimes one wing is missing. Distribution of intensity with velocity shows considerable variations. Time-scales from 20 to 200 s are exhibited in single events and in the complete set of events. Some events occur 2 or more times during our limited observing period and often a small but noticeable excess line width is found both before and after a major event.
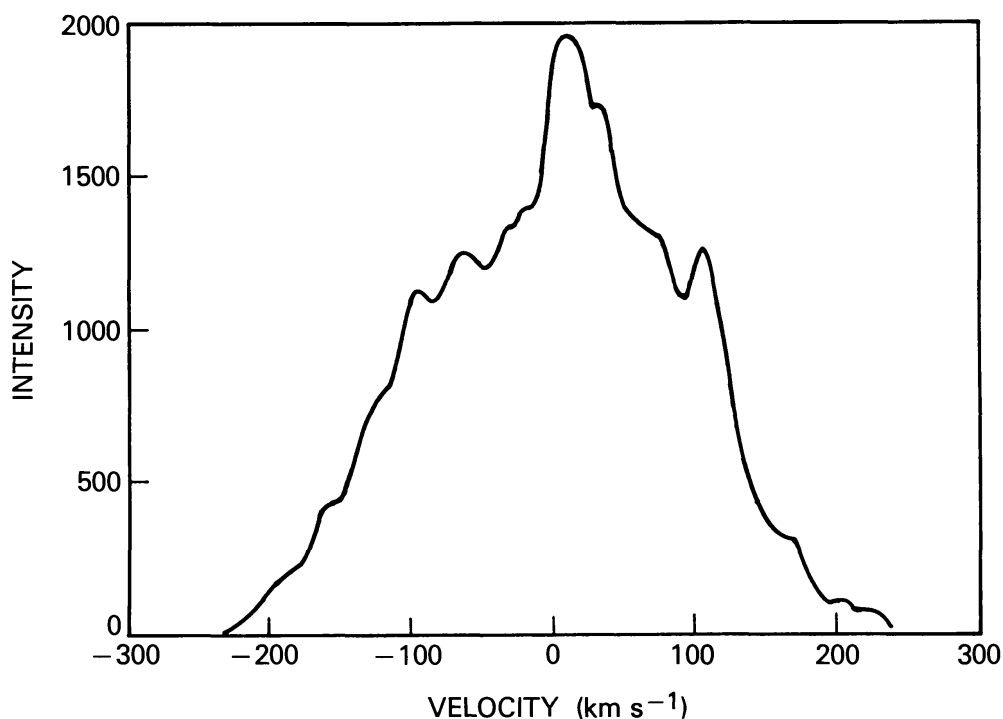
C IV λ1548 AND λ1550 PROFILE, EVENT 1660, PLATE 9 × 6

Fig. 15.   The profile of C IV during the maximum phase of event No. 6 (1660).

4. Physical Properties of Explosive Events

The physical properties of 82 explosive events observed in the HRTS-3 data have been measured and are presented here. Most of these measurements refer to profiles at the time of maximum brightness.

4.1. THE SIZES OF EXPLOSIVE EVENTS

Although the sizes of the explosive events are quite small, they often show considerable structure along the slit and with raster position. The full width at half maximum (FWHM) of brightness in both the blue and red wings along the slit have been measured and their distribution presented in Figure 16 for the blue wing (top) and for the red wing (bottom). The average FWHM for the blue wing is 1.5×10^3 km and for the red wing 1.7×10^3 km. These values have not been corrected for the finite spatial resolution of the instrument which is about $1''$. Such a correction would be quite minor for most of the events although there are some that have measured sizes near the instrumental resolution.

From a detailed analysis of the explosive event profiles it is clear that the positions of the blue and red wing emission along the slit are often displaced. The positions of the blue and red wing components have been measured and a histogram of the difference is presented in Figure 17. The distribution shown in Figure 17 has roughly the same FWHM of 1.5×10^3 km derived from the sizes of the red and blue components. It
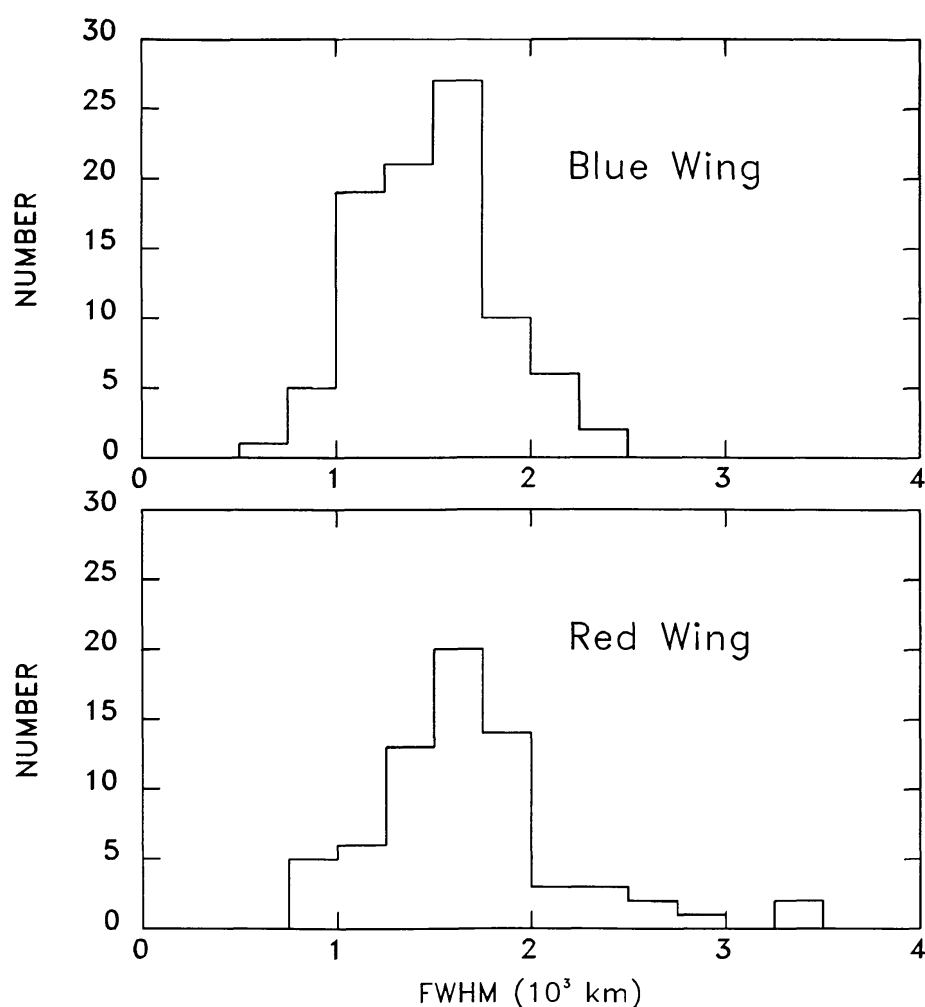
Fig. 16. A histogram of the spatial extent (FWHM) along the slit for the blue wing of C IV in explosive events (*top*) and similarly for the red wing (*bottom*).

appears that while the explosive events are indeed small, they have a measureable size of about 1.5×10^3 km and are not point sources.

4.2. C IV LINE PROFILES AND VELOCITIES

The explosive events have a high visibility in the HRTS spectra because their Doppler shifts are distinctly higher than the typical Doppler shifts observed in the quiet and active Sun, which are less than 20 km s^{-1}. Compared to the slower components, the explosive events are generally not bright. The maximum blue and red shifts observed at maximum phase have been measured and histograms of the values are presented in Figure 18. The average maximum blue shift is 108 km s^{-1} and the average maximum red shift is 114 km s^{-1}. The measured velocity distributions are distorted by several factors. First, there are a number of moderately strong chromospheric lines in the vicinity of the C IV lines at 1548 and 1550 Å. Near the 1548 Å C IV line, there are 2 Si I lines in the blue wing at 1547.4 Å with an equivalent blue shift of 155 km s^{-1} and a Si I line in the red wing at 1548.7 Å with an equivalent red shift of 98 km s^{-1}. Near the 1550 Å C IV line, there
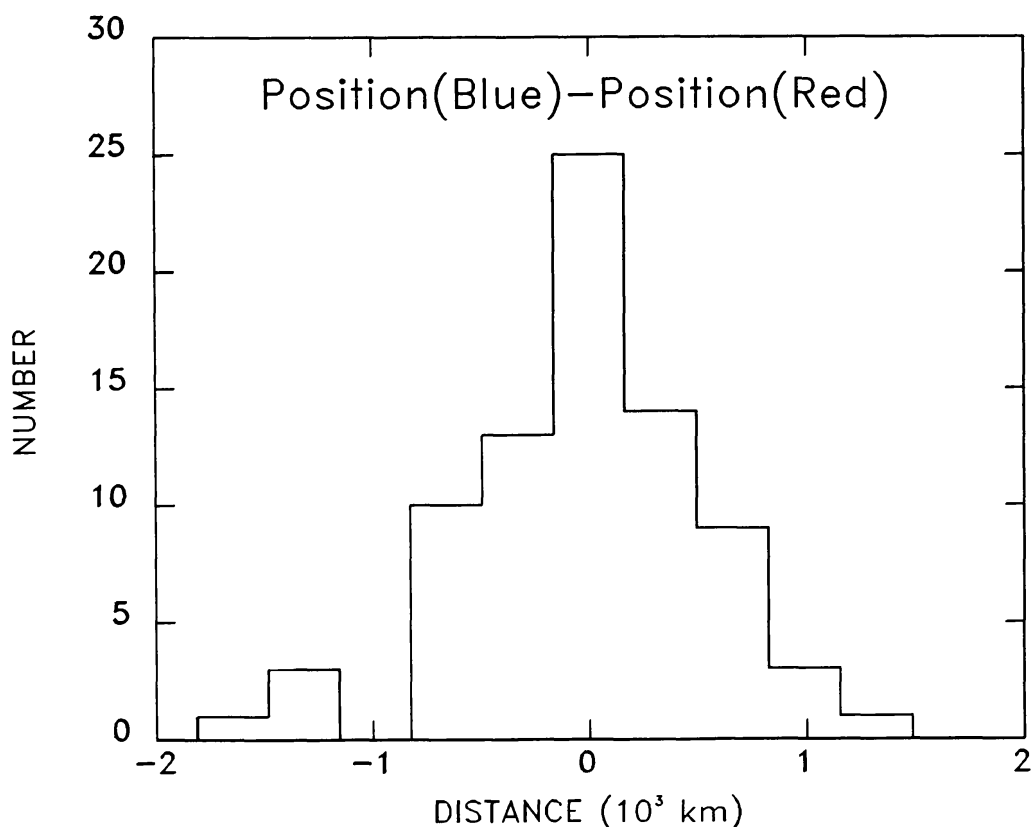
Fig. 17. A histogram of the difference in position along the slit between the blue wing and the red wing of explosive events.

is an Fe II line in the blue wing at 1550.3 Å with an equivalent blue shift of 99 km s^{-1} and a Si I line in the red wing at 1551.2 Å with an equivalent red shift of 90 km s^{-1}. These lines tend to make the profiles of the explosive events more visible at their equivalent Doppler shift positions and produce artificial peaks and valleys in the distribution curves. Second, explosive events with maximum velocities below 50 km s^{-1} blend into the much stronger background profiles and become indistinguishable. Since the background C IV profiles are red shifted, the lower velocity events in the blue wing are more likely to be visible and the decline in the number of events with blue shifts less than 70 km s^{-1} is probably real. The maximum blue-shift velocities fall within a limited range from 50 to 200 km s^{-1} with most near 100 km s^{-1}. This indicates that the explosive events are the result of a relatively uniform set of physical conditions.

Since the line-of-sight velocity is derived from the observed Doppler shift, the latitudinal variation in the observed velocity should provide information on the relative amount of vertical and horizontal flows present in the explosive events. In other words, measurements near the limb determine the velocity components tangential to the solar surface and measurements near disk center determine the velocity components normal to the solar surface. In Figure 19 the maximum blue-shift velocity has been plotted as a function of heliographic latitude. This data indicate that the line-of-sight velocity is independent of the viewing angle so that, on average, each event produces roughly equal amounts of horizontal and vertical flows.
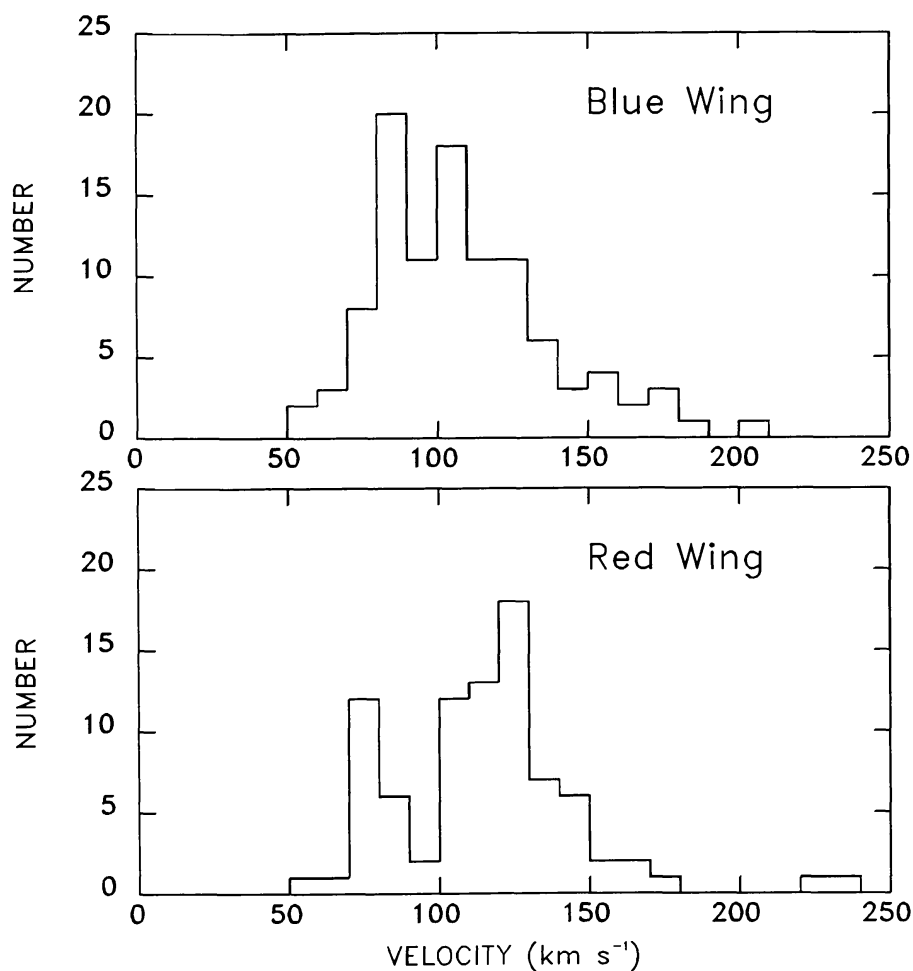
Fig. 18.   A histogram of the maximum C IV blue-shift velocity in explosive events (*top*) and a histogram of the maximum C IV red-shift velocity (*bottom*).

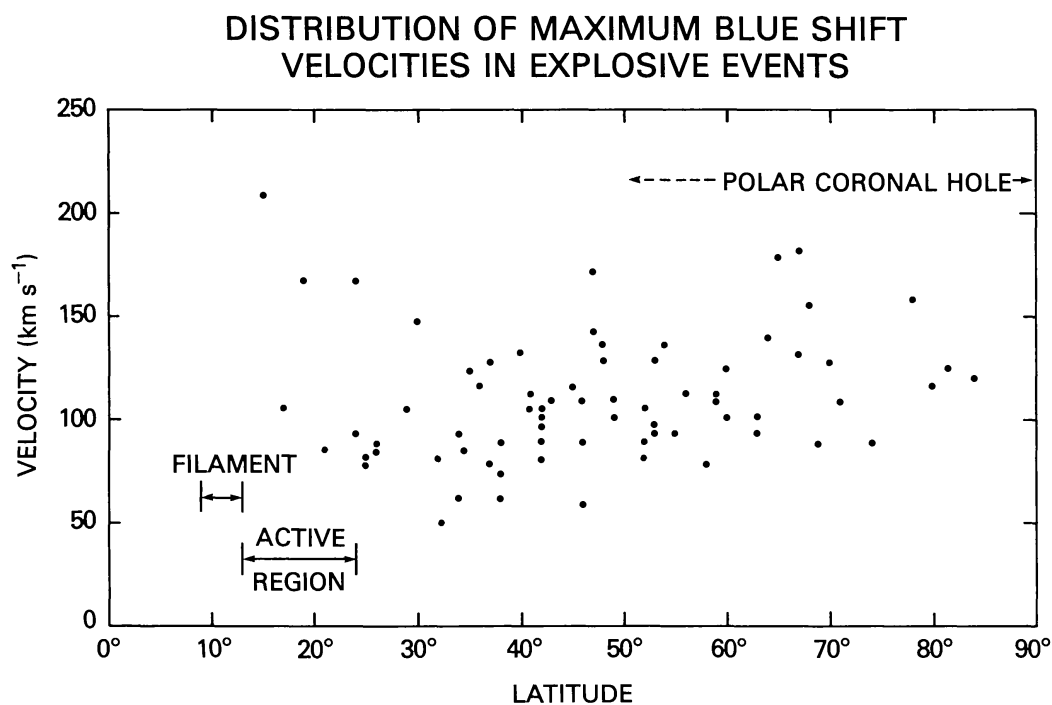## DISTRIBUTION OF MAXIMUM BLUE SHIFT VELOCITIES IN EXPLOSIVE EVENTS

Fig. 19.   Maximum C IV blue-shift velocity plotted against the solar latitude of the explosive event.

From the observed integrated line intensities in the C IV line wing components, it is possible to derive the volumetric emission measure $(n_e^2 V)$ at 10^5 K, where n_e is the electron density and V the volume. Since the HRTS slit is $1''$ wide, it is somewhat smaller than the extent of the typical explosive event and the intensities derived from the profiles refer only to those parts of the explosive events that are in the field of view of the slit. We have corrected these values by a factor equal to the ratio of the estimated area of each explosive events to the area of the event that is covered by the slit. We have assumed that actual area is that of a circle whose diameter is given by the FWHM of the event along the slit. This correction factor is generally between 1 and 2 but can be as large as 3.5. The distribution of emission measures derived from the corrected intensities is shown in Figure 20 for both the blue and red wings. The average emission measure for both the red and blue wings is 4×10^{41} cm^{-3}.
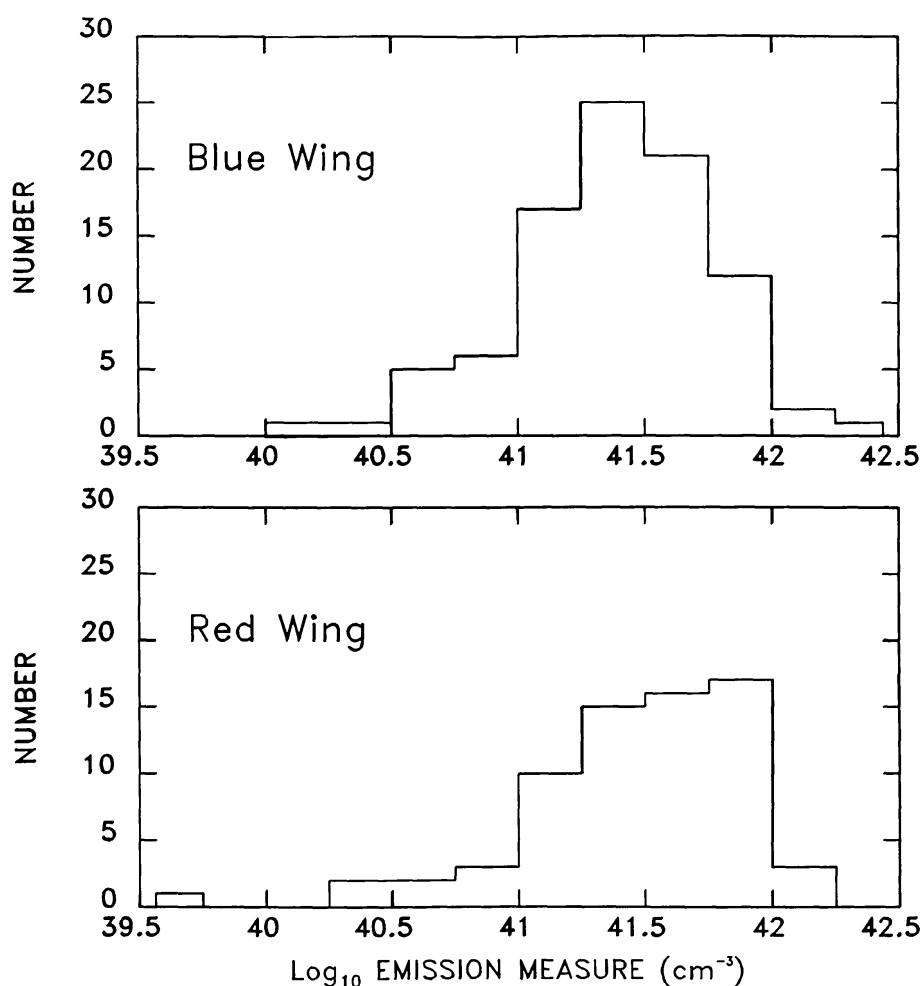
Fig. 20. A histogram of the emission measure $(n_e^2 V)$ of the C IV blue wing at maximum phase in explosive events (*top*) and similarly for the red wing (*bottom*).

In general, the profiles of the explosive events are not symmetric. To display this characteristic statistically, the corrected integrated intensities of the red and blue wing components have been measured at maximum phase and a histogram of the ratios of the red wing to the blue wing intensity has been plotted in Figure 21. The large number

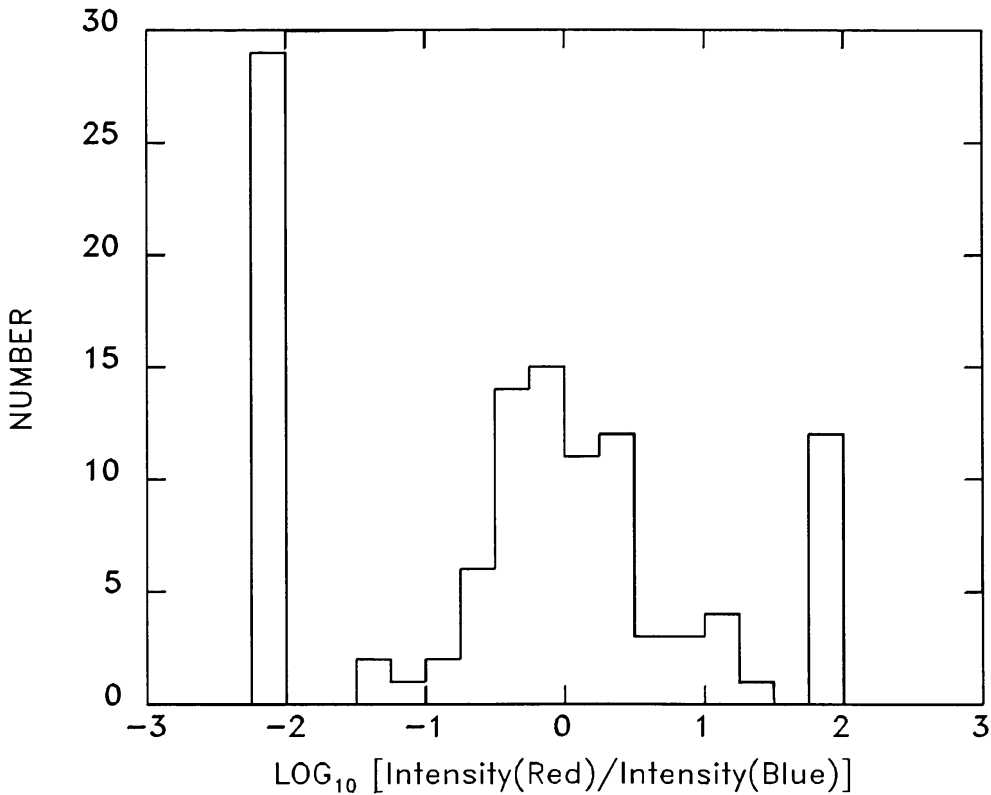Fig. 21. A histogram of the ratio of the integrated intensity in the red wing to the integrated intensity in the blue wing at maximum phase.

of events at the two extremes correspond to the number of events where only one wing is strong enough to be measured. The events with dominant blue wings outnumber the events with dominant red wings by about 3:2.

The shape of the line profiles shows considerable variation from event to event. At least 3 general profile shapes can be discerned. First, there are those where the intensity falls off monotonically from low to high velocities, whether in the blue, red or both line wings. This is seen in examples 3 (Figures 7 and 8). For others, the intensity remains fairly constant over a range of velocities, as in example 2 (Figure 6). In examples 1 (Figure 2) and 5 (Figure 13), the intensity peaks at some intermediate velocity below the peak velocity. These various profile shapes are most likely the result of varying combinations of ordered and turbulent flow velocities.

4.3. TIME-SCALES

From the various examples, it is clear that explosive events evolve on time-scales ranging from 20 to 200 s. The 82 explosive events in our data set have been examined in order to quantify time-scales for each event. The problem is complicated by the fact that many events evolve on at least two different time-scales, such as in those frequent cases where the explosive event consists of short-lived high-velocity event superposed on a longer-lived, lower velocity event. For this study we have focused on the short-lived, high-velocity component. From a visual inspection of the spectra displayed in the format used

in Figure 1, time-scales for each event have been estimated. They correspond to a visual estimate of the FWHM of the intensity variation for the longer events and in the case of the shortest-lived events, the number of consecutive rasters the event was seen on. A histogram of the lifetimes is presented in Figure 22. The average lifetime is 60 s. There does not appear to be any strong difference between the lifetimes of the red and blue wing. These results differ from those of Brueckner and Bartoe (1983) who derive an average lifetime of 40 s and present a distribution of lifetimes that peaks at 20 s. Some of this can probably be attributed to the use of spectra obtained before the pointing completely stabilized. This would tend to increase the number of short-lived events found. The rest can probably be attributed to differences in methodology.
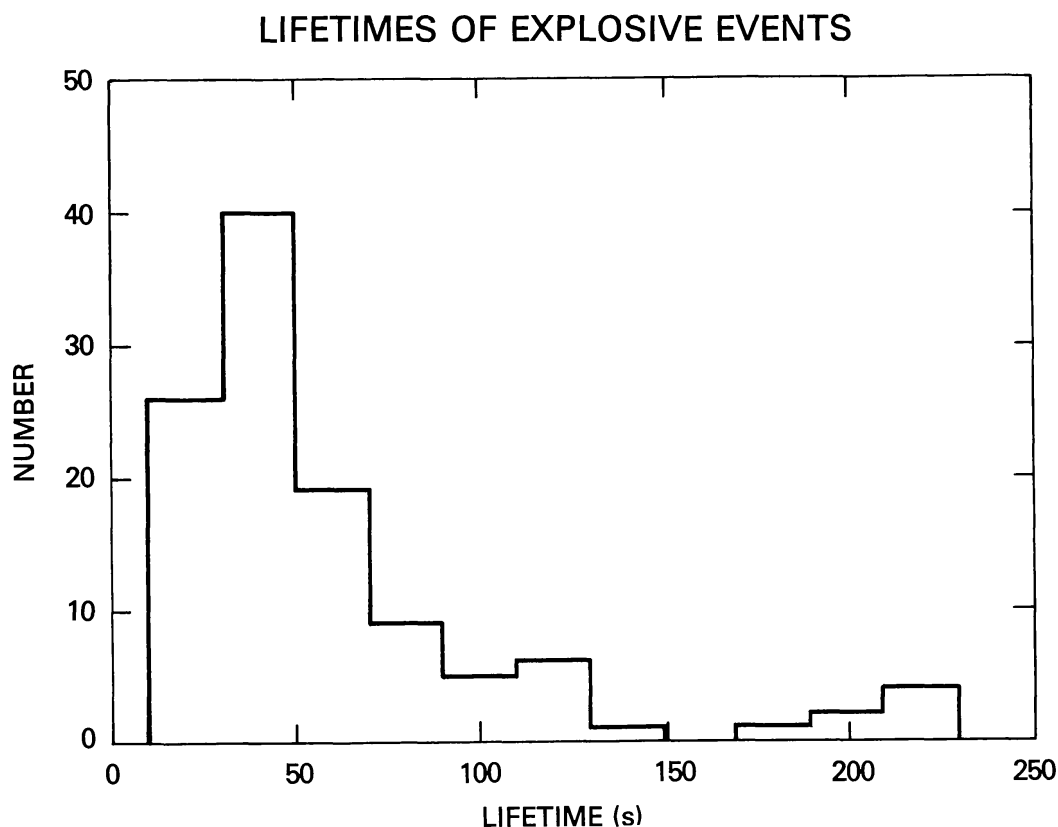

Fig. 22. A histogram of the lifetime of explosive events.

4.4. APPARENT VELOCITIES

It is possible to assemble the time series of spectra with an accuracy that allows one to measure the motion of plasmas along the slit with velocities as low as 5 km s^{-1} in a feature that lasts 200 s or as low as 20 km s^{-1} in a typical explosive event which lasts 60 s. Aside from example 5, no significant evidence is found for apparent velocities along the slit. Because of the lack of a latitudinal dependence in the velocities which implied considerable horizontal, as well as vertical components, one would expect to see some evidence for motions of these plasmas along the solar surface at velocities of 100 km s^{-1} which should be easily detectable.

4.5. ACCELERATION

The acceleration of plasma during an explosive event is not a quantity that can always be measured unambiguously. For example, we have pointed out that the evolution of some profiles can be explained simply by changes in the intensity of a profile of fixed shape. There are also many cases where a 100 km s^{-1} explosive event suddenly appears in one raster and was not seen in the previous raster 20 s earlier. From such data accelerations of about 5 km s^{-2} are derived. Brueckner and Bartoe (1983) directly measured a similar value in the acceleration of a large jet.

Fig. 23.   The two-dimensional positions of the sites of the explosive events in relationship to the images of the total line intensity in Fe II λ1563 and C IV λ1548 and λ1550 to the left and right, respectively, for the half of the HRTS slit near the limb.

4.6. Spatial distribution

In Figures 23 and 24 images of the line intensity of Fe II $\lambda1563$ and C IV $\lambda1548$ and $\lambda1550$ are displayed on either side of an image depicting the locations of the explosive events. The Fe II and C IV intensity images have been discussed in detail before (Dere, Bartoe, and Brueckner, 1986a) and the raster line numbers have been retained for reference to the discussion in that paper. The observations are located along a solar radius from the limb to $800''$ inside the limb. The solar limb is indicated by the bright regions near raster lines 50 and the large raster line numbers are near Sun center. Portions of a decaying active region are located between raster line numbers 1340 and 1750 and a filament is
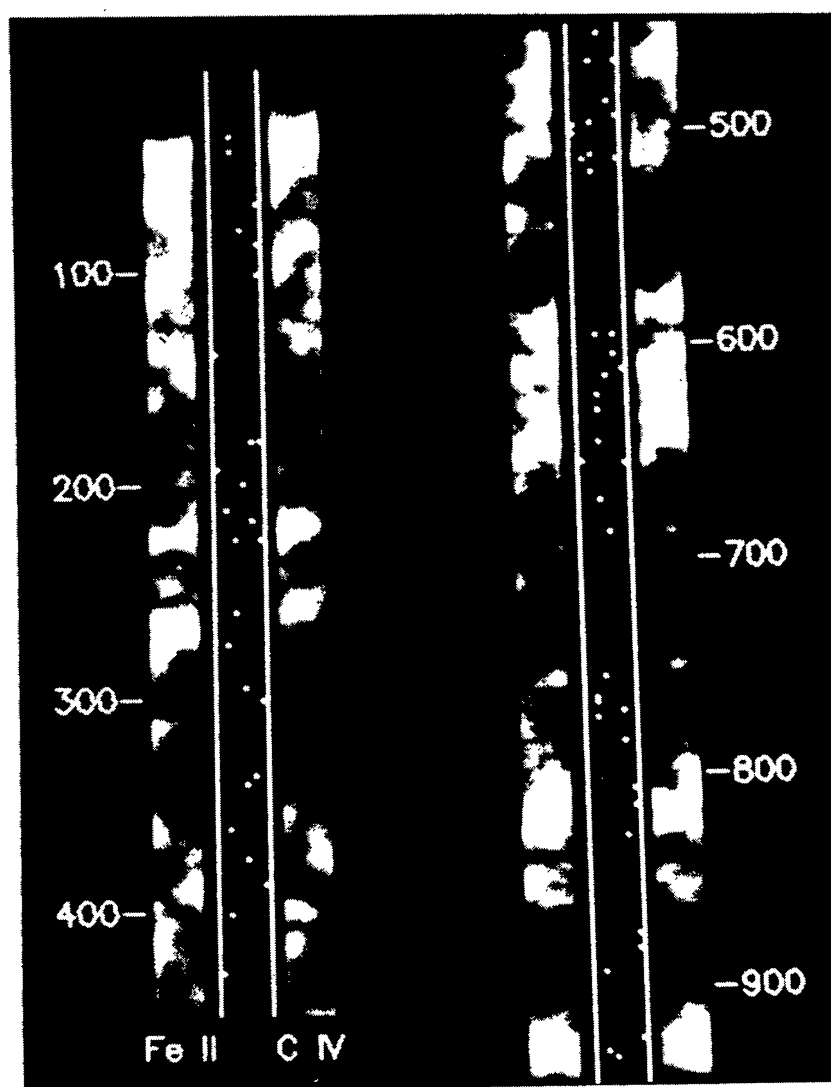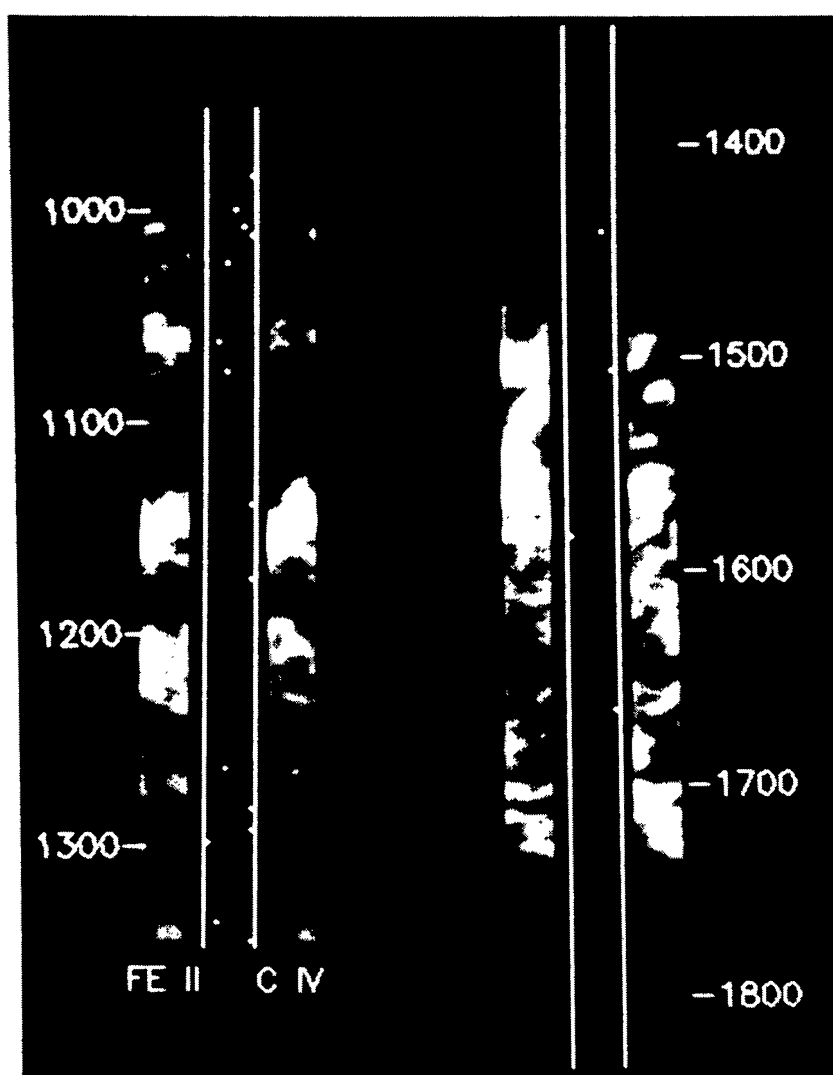

Fig. 24.   The two-dimensional positions of the sites of the explosive events in relationship to the images of the total line intensity in Fe II $\lambda1563$ and C IV $\lambda1548$ and $\lambda1550$ to the left and right, respectively, for the half of the HRTS slit near Sun center.

located at raster lines above 1750. A histogram of the solar latitude of the sites of the explosive events is presented in Figure 25. These three figures suggest that there may be some correlation between the explosive events and network structures, indicated by intense Fe II and C IV emissions, particularly at mid latitudes. The distribution of pair separations (the distance between two event locations) has been calculated and compared with that expected from a random distribution of explosive events. There are no indications of deviations from a random distribution that could not be explained by the tendency of events in this ensemble to occur at mid latitudes.
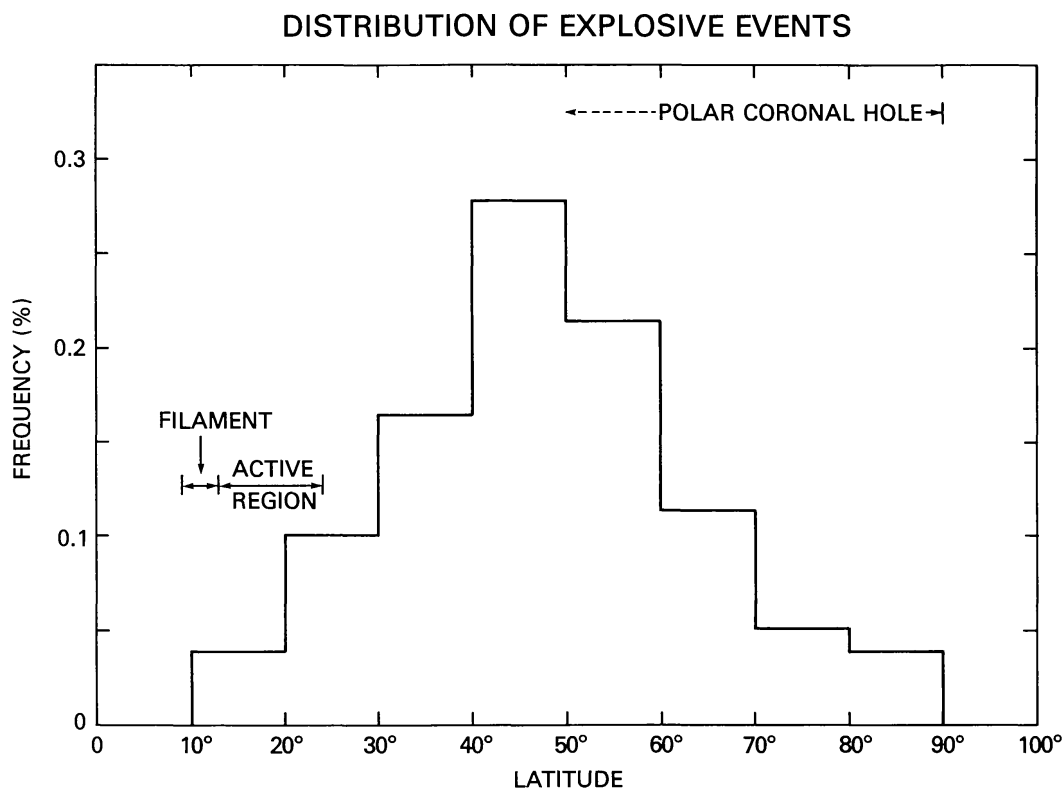
DISTRIBUTION OF EXPLOSIVE EVENTS

Fig. 25.   The distribution of the latitudes of the sites of the explosive events.

4.7. BIRTHRATE

Calculations of an average birthrate for explosive events from this data set could be distorted by the presence of different large scale features such as an active region, a filament, and a polar coronal hole in the field of view. We will limit the present calculation to regions of the quiet Sun and the polar coronal hole. It is our suspicion that the explosive events are related to the interaction of magnetic flux tubes which is likely to be suppressed in a filament and a decaying active region. In the polar coronal hole region (55–90° latitude), 25 explosive events were seen during a 220 s observing period. Using the formula birthrate = (number observed)/[(field of view) × (observing time)], we derive a birthrate in the coronal hole of 4×10^{-21} cm^{-2} s^{-1}. Although one could attempt some minor corrections to the calculated rate, this formula is appropriate

to use since the observing time is longer that the typical lifetime of the individual events. In the quiet region (24–55° latitude), 53 explosive events were seen and a birthrate of 1×10^{-20} cm^{-2} s^{-1} is calculated. This latter value is equivalent to a full disk quiet Sun birthrate of 600 s^{-1} and is comparable to the Brueckner and Bartoe (1983) value of 750 s^{-1}. Cook *et al.* (1988) derived a much lower birthrate (44 s^{-1}) but their value was based on single rasters although of a much larger field of view.

4.8. MASS AND KINETIC ENERGY

The total mass and kinetic energy are important physical characteristics of the explosive events and can be derived from the observed parameters previously discussed. The total mass M is given by

$$M = m_p n_e V = m_p [(n_e^2 V) V]^{1/2}, \tag{1}$$

where m_p is the proton mass, V the volume and $(n_e^2 V)$ represents the volumetric emission measure. The total kinetic energy KE is given by

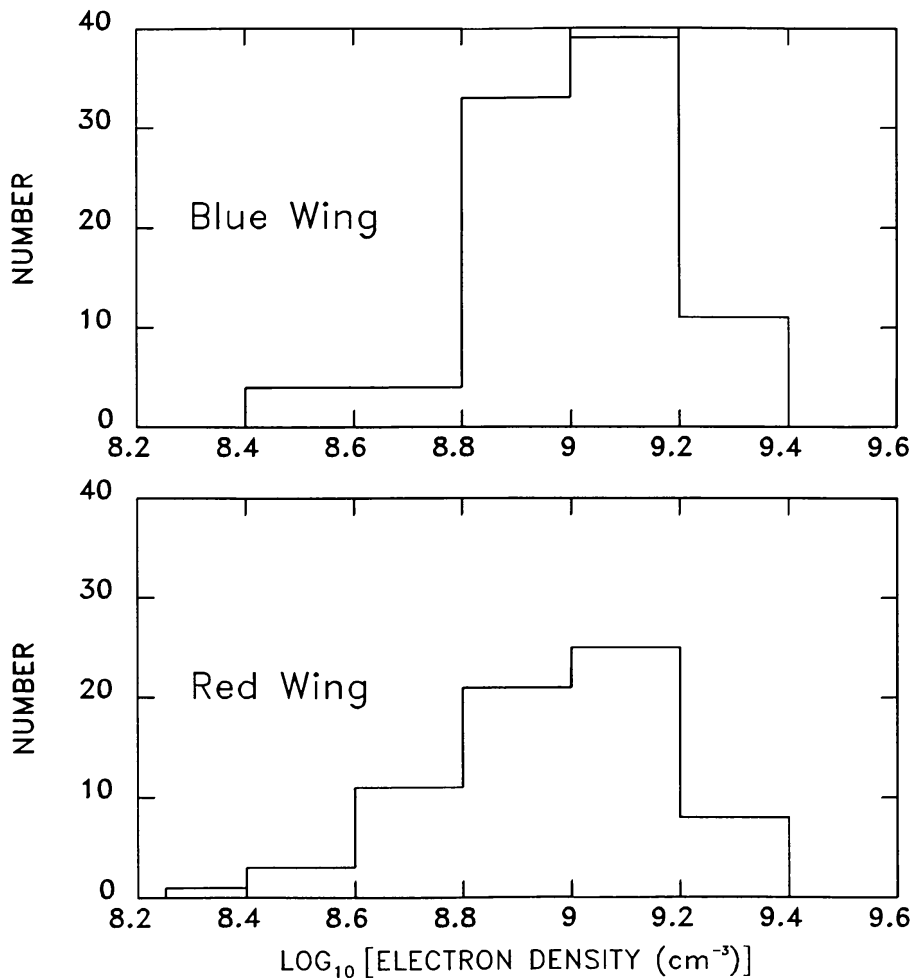$$KE = \tfrac{1}{2} M v^2, \tag{2}$$

Fig. 26. A histogram of the average electron density (n_e) derived for the C IV blue wing at maximum phase in explosive events (*top*) and similarly for the red wing (*bottom*).

where v is the velocity. Before calculating these quantities, it is important to consider the possible effect that the existence of unresolved fine structure would have on the derived quantities M and KE. Previously, an examination of the densities and emission measures of apparently resolved structures in the quiet Sun led to the conclusion that less than 1% of the observed volume was filled with C IV emitting material (Dere *et al.*, 1987). If the actual volume of C IV emitting material is given by fV, where V is the apparent volume and f is the filling factor which is less than or equal to unity, the total mass $M = m_p(n_e^2 V)^{1/2} (fV)^{1/2}$. Consequently, the total mass and kinetic energy are maximized for the case where there is no unresolved fine structure ($f = 1$). Another way to examine this question is to calculate the apparent average electron density as a function of the fill factor $<n_e> = (n_e^2 V)^{1/2}/(fV)^{1/2}$. The apparent average density is minimized for a fill factor of unity. If the density can be determined by other methods, such as density sensitive line intensity ratios, then a comparison of the two would determine the fill factor. In Figure 26 the distribution of electron densities for the blue and red wings of the explosive events for an assumed fill factor of unity are displayed. The average electron density for the blue wing is $1.1 \times 10^9 \, \text{cm}^{-3}$ and the average
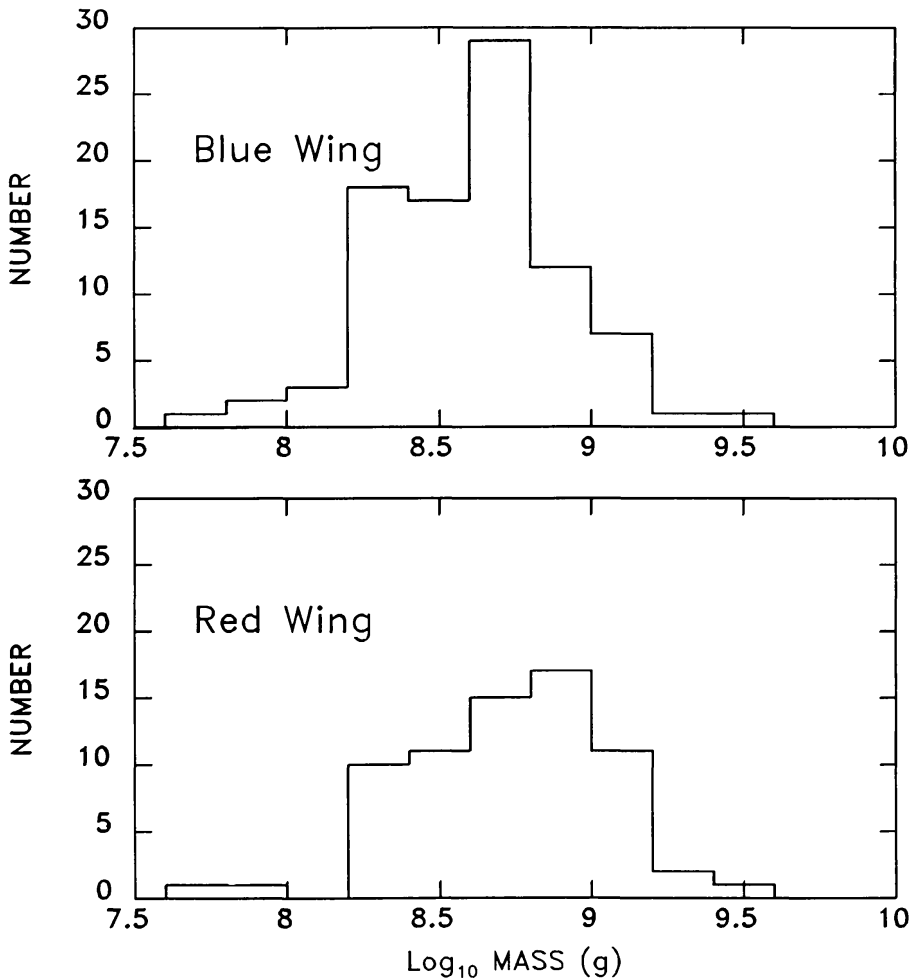

Fig. 27. A histogram of the total mass M for the C IV blue wing at maximum phase in explosive events (*top*) and similarly for the red wing (*bottom*).

electron density for the red wing is $1.0 \times 10^9 \, \mathrm{cm}^{-3}$. If quiet Sun densities, typically $10^{10} \, \mathrm{cm}^{-3}$ at 10^5 K, are appropriate for explosive events, then a fill factor of 1% is indicated. On the other hand, C IV is formed in only a limited temperature range around 10^5 K. Brueckner and Bartoe (1983) considered the integrated emission measure for temperatures between 2×10^4 and 2×10^5 K and derived an average density of $10^{10} \, \mathrm{cm}^{-3}$. This result indicated that perhaps the fill factor for C IV is 1% but that the volume of the explosive events is filled with material at a variety of temperatures. Since the full range of spectral lines were not recorded in this rocket flight, the total mass M and kinetic energy KE have been calculated by means of Equations (1) and (2) under the assumption that the fill factor is unity and with the understanding that the derived values could be an order of magnitude low. The volume is taken to be that of a sphere having a diameter equal to the FWHM extent of the event along the slit. The distribution of these values are displayed in Figures 27 and 28 for the mass and kinetic energy, respectively. The average mass in the blue wing is 5×10^8 g and the average mass for the red wing is 7×10^8 g. The average kinetic energy in the blue wing is 6×10^{22} erg and the average kinetic energy in the red wing is 5×10^{22} erg.
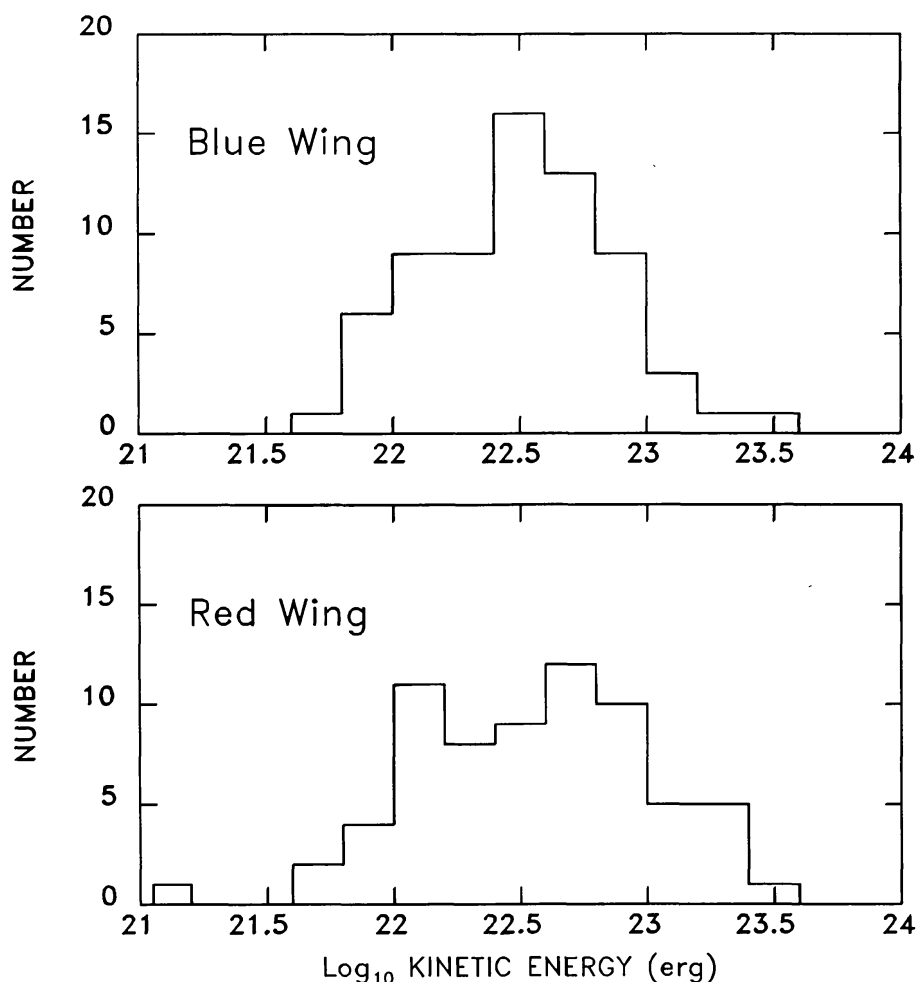

Fig. 28.   A histogram of the total kinetic energy KE for the C IV blue wing at maximum phase in explosive events (*top*) and similarly for the red wing (*bottom*).

5. Discussion

Although Brueckner and Bartoe (1983) originally called these high-velocity events 'turbulent' events, we have referred to them throughout this paper as 'explosive events'. Because the red and blue components of the high velocity profiles are often separated along the slit, the overall profile cannot be explained by turbulence alone, but significant mass motions must also be involved. The explosive events give the impression of explosions in that isotropic mass motions are nearly instantaneously produced in a small volume. The events are small although not point-like, the velocities appear to be isotropic as evidenced by the lack of correlation of the velocity with solar latitude and many events show large accelerations in the 20s between observations. Thus, the term 'explosive event' implies many of the properties observed in these events, if not each event in detail, and can be used in a meaningful way.

One would expect the explosive events to be driven by changes in the magnetic field, as is suspected to be the case with most forms of solar activity. Extrapolations of the observed photospheric field provide the only clue as to the field configuration at higher levels. The series of HRTS observing programs have not been very fortunate in obtaining near simultaneous magnetograms, including the HRTS-3 rocket flight. The HRTS-5 flight was successful in having simultaneous photospheric magnetograms and the analysis and reduction of these data sets is in progress. Otherwise, there are only two cases where explosive events can be related to magnetic changes, in both cases emerging magnetic flux. Brueckner *et al.* (1988) report highly exceptional explosive events seen during the Spacelab-2 operations in August 1985 that were related to an emerging flux region near a sunspot. This explosive event was exceptional both in its extent ($30''$) and its velocity (up to $300 \ \text{km s}^{-1}$). Evidence for the emerging flux was seen in both photospheric magnetograms and in the classic Hα arch filament systems commonly associated with emerging magnetic flux. A more typical but relatively long-lived explosive event was found a day earlier during the Spacelab-2 mission at the edge of the same sunspot where magnetograms from the Meudon solar observatory showed the emergence of opposite polarity magnetic flux. Porter *et al.* (1987) showed that microflares (or explosive events) observed in the SMM data were associated with small magnetic bipoles. It should be possible to confirm this result with the recent HRTS-5 data set.

One aspect of the observed properties of the explosive events that is hard to explain is the lack of detectable apparent motions of the high velocity emission across the solar surface. Plasmas with speeds of $100 \ \text{km s}^{-1}$ should travel 6×10^3 km or $8''$ during an average lifetime of 60 s. Such a motion, even if only some component were directed across the solar surface, should be detectable. One explanation is that plasma is being accelerated through $100 \ \text{km s}^{-1}$ at the same time that it is being heated (or cooled) through 10^5 K, in a fixed region. Consequently, when the plasma leaves the acceleration site, it is not at a temperature visible in C IV.

Brueckner and Bartoe (1983) suggested that the high velocity jets, an apparently different class of events than discussed here, could provide the mass needed to supply the solar wind. We examine here the mass that is involved in the explosive events and

compare it with the net outflow of mass in the solar wind. The solar mass loss dM/dt potentially carried off by the explosive events is given by $dM/dt|_{EE} = MBA_{\odot}$, where M is the average mass involved in each event, B the birthrate, and $A_{\odot}$ the area of the solar surface. With $M = 5 \times 10^8$ g and $B = 1 \times 10^{-20}$ cm^{-2} s^{-1} (the quiet-Sun value), $dM/dt = 3 \times 10^{11}$ g s^{-1}. The average mass loss in the solar wind can be calculated from $dM/dt|_{SW} = \mu NVA = 3.5 \times 10^{11}$ g s^{-1} (Schwenn, 1983), where μ is the proton mass, NV the proton mass flux, and A the area of a sphere at 1 AU. Clearly, when examined on a global scale, the explosive events must be considered a potential source of the solar wind mass flux. As we have discussed previously, our estimate for the mass in the explosive events is an upper limit on the mass of C IV temperature material involved, although it may be much less that the total mass involved when the complete range of temperatures is considered.

Porter *et al.* (1987) and Parker (1988) suggest that explosive events belong to a class of events called 'microflares' or 'nanoflares' that are the source of coronal heating. The case for this seems to be largely based on a comparison of the energy available in microflares and the energy lost by radiation from the corona. An alternative suggestion is that the explosive events occur at the locations of emerging magnetic flux and that because of the frozen-in nature of the plasma, they remain isolated from other coronal structures. It is hard to see how the explosive events can be responsible for heating typical solar structures. The HRTS-3 spectra used to study the explosive events also show the temporal development of the quiet transition with a temporal resolution of 20 s over a 220 s interval. The great majority of these structures show very little variation over this observing period. If these quiet structures are to be heated by microflares, they must occur at intervals commensurate with the radiative loss time. The radiative loss time for C IV can be taken as the time in which the radiative losses at 10^5 K cool the plasma enough to produce a substantial dimming in C IV. A spectral line such as C IV is typically formed over a temperature range of a factor of 2, so a change in temperature of a factor of $\sqrt{2}$ would considerably reduce the emission of C IV. Equating the change in thermal energy at constant pressure to the radiative losses over a time Δt,

$$5/2(n_e + n_p)k\Delta T = n_e^2 \Lambda(T)\Delta t, \tag{3}$$

with $n_e = n_p = 10^{10}$ cm^{-3}, $\Delta T = T/\sqrt{2} = 10^5 K/\sqrt{2}$ and $\Lambda(T) = 6 \times 10^{-22}$ cm^{-3}, we find $\Delta t = 8$ s. An energy of 6×10^{23} erg released every 3 s would then maintain the temperature in a (1500 km)^3 volume. If the heating were supplied by explosive events, then they would have to occur essentially constantly. This is certainly contradicted by the observations which show that explosive events to be common but nevertheless special events. Nor do they necessarily occur in the bright network structures where the radiative losses are highest. Further, the explosive events appear to be the result of processes that produce large amounts of kinetic energy over distinct but relatively large spatial scales which is probably difficult to convert to thermal energy in quiescent structures. Davila (1987), Einaudi and Mok (1987), and Dere (1989) have proposed mechanisms where the typical nonthermal motions (20 km s^{-1}) can be converted into thermal energy and maintain transition region and coronal plasmas.

References

Brueckner, G. E. and Bartoe, J.-D. F.: 1983, *Astrophys. J.* **272**, 329.

Brueckner, G. E., Bartoe, J.-D. F., Cook, J. W., Dere, K. P., Socker, D., Kurokawa, H., and McCabe, M.: 1988, *Astrophys. J.* **335**, 986.

Cook, J. W., Lund, P. A., Bartoe, J.-D. F., Brueckner, G. E., Dere, K. P., and Socker, D. G.: 1988, in J. L. Linsky and R. E. Stencel (eds.), 'Cool Stars Stellar Systems and the Sun', *Lecture Notes in Physics* 291, Springer-Verlag, Berlin.

Davila, J. M.: 1987, *Astrophys. J.* **317**, 514.

Dere, K. P.: 1989, *Astrophys. J.* **340**, 599.

Dere, K. P., Bartoe, J.-D. F., and Brueckner, G. E.: 1984, *Astrophys. J.* **281**, 870.

Dere, K. P., Bartoe, J.-D. F., and Brueckner, G. E.: 1986a, *Astrophys. J.* **305**, 947.

Dere, K. P., Bartoe, J.-D. F., and Brueckner, G. E.: 1986b, *Astrophys. J.* **310**, 456.

Dere, K. P., Bartoe, J.-D. F., Brueckner, G. E., Cook, J. W., and Socker, D. G.: 1987, *Solar Phys.* **114**, 22.

Einaudi, G. and Mok, Y.: 1987, *Astrophys. J.* **319**, 520.

Parker, E. N.: 1988, *Astrophys. J.* **330**, 474.

Porter, J. G., Moore, R. L., Reichmann, E. J., Engvold, O., and Harvey, K. L.: 1987, *Astrophys. J.* **323**, 380.

Schwenn, R.: 1983, in M. Neugebauer (ed.), *Solar Wind Five*, NASA Conference Publication 2280.